

Powering Up the Oxygen Reduction Reaction through the Integration of O₂-Adsorbing Metal–Organic Frameworks on Nanocomposite Electrodes

Gonzalo E. Fenoy,^{†,‡} Juliana Scotto,^{†,§} Julio Azcárate,^{||} Matías Rafti,^{*,†} Waldemar A. Marmisollé,^{*,†} and Omar Azzaroni[†]

[†]Instituto de Investigaciones Físicoquímicas Teóricas y Aplicadas (INIFTA), Departamento de Química, Facultad de Ciencias Exactas, Universidad Nacional de La Plata (UNLP), CONICET 64 and 113, La Plata 1900, Buenos Aires, Argentina

[‡]Instituto de Investigación e Ingeniería Ambiental, Universidad Nacional de San Martín, 25 de mayo y Francia, 1 piso, San Martín 1650, Buenos Aires, Argentina

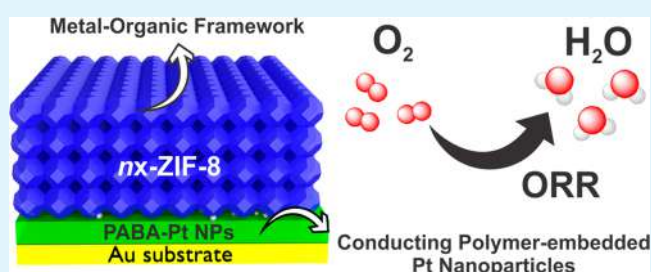
[§]Instituto de Ciencias de la Salud, Universidad Nacional Arturo Jauretche, Av. Calchaquí 6200, Florencio Varela 1888, Buenos Aires, Argentina

^{||}Centro Atómico Bariloche (CAB), CONICET - Avenida Bustillo 9500, San Carlos de Bariloche 8400, Río Negro, Argentina

Supporting Information

ABSTRACT: Oxygen reduction reaction (ORR), essential in many energy conversion devices, takes particular relevance in facing the increasing global demand for clean energy sources and vectors. In this context, desirable features for ORR-based electrochemical cells are operability under environmentally friendly conditions, such as pH 7 biocompatible electrolytes, and the usage of relatively low electrocatalyst loadings. On the other hand, the improvement of the cathode performance in neutral solutions is commonly focused on the development of electrocatalyzers for reducing the ORR overpotential. In this work, we took advantage of the possibilities brought by a novel strategy toward construction of complex interfacial architectures, the so-called “nanoarchitectonics” approach. In order to achieve enhanced ORR currents and reduced overpotentials, we combined three different building blocks with defined functionalities: a conducting polymer (CP) nanofilm (the connecting electroactive matrix), well dispersed Pt-nanoparticles (the electrocatalyzer), and a layer of a Zn-based metal–organic framework (MOF) nanocrystals (the in situ oxygen reservoir). The sequential synthetic procedure includes the electrosynthesis of a polyaniline-like electroactive film, the synthesis of Pt nanoparticles within this film, and the deposition of a layer of MOF nanocrystals, which adds micro/mesoporosity to the assembly. The incorporation of the MOF nanocrystals layer incorporates two fundamental aspects: it allows for the ionic transport through its interparticle interstices, and also selectively promotes the O₂ preconcentration, which is then available for the ORR on the embedded catalytically active metallic nanoparticles. The rational integration of these blocks yields a functional interfacial architecture for enhanced ORR currents in eco-friendly neutral pH KCl solutions.

KEYWORDS: oxygen reduction reaction, conducting polymers, Pt nanoparticles, metal–organic frameworks, polyaniline, electrocatalysis, nanoarchitectonics



INTRODUCTION

The increasing global demand for energy is only expected to accelerate in the next decades, pushing forward research efforts focused on the quest for renewable energy sources and its coupling to electrochemical conversion devices.¹ Electrochemical energy conversion and storage (e.g., using metal-air batteries, or fuel cells) uses a water splitting reaction, which involves the hydrogen evolution reaction (HER), the oxygen evolution reaction (OER), and the oxygen reduction reaction (ORR). Technologies relying on the above reactions depend on the availability of catalytic materials for reducing the existing overpotentials, and thus rendering the overall

processes economically and technologically feasible.² Desirable features of such catalysts would also include the possibility of long-term operation under environmentally friendly conditions, and the synthesis from relatively inexpensive precursors. Platinum is the single most employed (and efficient) cathode material for the catalyzed electrochemical ORR, with significant drawbacks being its low availability, high price, and relatively concentrated market. Advances have been

Received: June 25, 2018

Accepted: September 10, 2018

Published: September 10, 2018

achieved by introducing the use of various different porous supports which reduce diffusional constraints, and by reducing the Pt loadings needed for operation with the introduction of dispersed (and more active) Pt nanoparticles (Pt-NPs).^{3–5} Recently, conducting polymer-supported Pt-NPs have attracted much attention due to the presence of tunable chemical structures through redox reactions, and different moieties in the main polymeric chains. Among CPs, polyaniline (Pani) appears as one of the most explored options due to the presence of an amine moiety on its polymeric backbone and its high reduction potential, both features which yield great chemical versatility and allow for the growth of Pt NPs, even under mild conditions.^{6–9} An interesting approach to the positioning of metal NPs on CPs for their use as composite electrocatalysts, consists of taking advantage of the available redox states in order to perform an *in situ* reduction of loaded Pt precursors, thus avoiding the use of harsher conditions (e.g., high temperatures or hazardous reducing agent).¹⁰ Pani/Pt-NPs films produced by this method were shown to be uniform, with high areal Pt loading, and featured high current densities, good durability for the methanol oxidation reaction, and excellent carbon monoxide tolerance.^{7,8}

Traditionally, inorganic porous materials (e.g., carbon based) have been used as supports for electroactive materials such as Pt or CPs, due to their high stability and surface area, which makes possible the storage of energy carriers while also allowing for efficient mass and charge transport. Another promising use has become available, with the appearance of a relatively new class of porous coordination materials, consisting of infinite noncovalently linked nets of metal (or metal cluster) nodes and organic multidentate linkers, the so-called metal organic frameworks (MOFs).^{11,12}

Among the many advantages that cause MOFs to outperform traditional porous materials for diverse applications, the following can be highlighted: very high surface areas, well-ordered pore structures with tunable sizes and topologies, and the possibility of carefully selecting pore wall chemistry (either using predefined construction blocks or via post-synthetic modification).^{13–16} Naturally, these interesting features have triggered the appearance of multiple studies reporting the use of MOFs for various applications such as solar cells for photoelectric energy conversion,^{17,18} adsorption of energetically and environmentally relevant gases,¹⁹ cathode materials for Li–O₂ cells,²⁰ CO₂ capture, and photocatalytic conversion,^{21,22} and composite catalyst synthesis via different approaches (e.g., encapsulation of metallo-porphyrins,²³ enzymes,^{24,25} metal–organic polyhedrals,²⁶ or metal nanoparticles²⁷). Although most MOFs are mainly insulating (i.e., its use as electrodes or semiconductive surfaces needs careful thickness control²⁸ or previous steps aimed to increase the conductivity, such as integration with graphene oxide,^{29,30} metal nanoparticles,³¹ or partial/total carbonization³²), there are few recent examples of conductive MOFs³³ with redox active sites, e.g., for the electrochemical ORR.^{34,35}

On the other hand, although ORR has been extensively studied in H₂SO₄ or KOH solutions,⁴ the improvement of this reaction in neutral media also results in major practical importance for devices such as biofuel cells³⁶ or microbial fuel cells,^{37,38} which are supposed to work in biocompatible conditions. However, the performance of this reaction at pH 7 presents additional challenges arising from the low concentrations of H⁺ and OH[–], which are involved in the ORR mechanism. Hence, the development of strategies to

improve the efficiency of this electrochemical reaction at neutral pH has both basic and technological significance.

Inspired by different composite materials exploiting MOFs selective gas adsorption for reaction enhancement (e.g., reduction reactions enhanced by incremented H₂ storage,^{39,40} or catalyzed carbon dioxide reduction reaction enhancement^{41–43}) we have recently showed that the deposition of a ZIF-8 (an archetypal member of the zeolitic imidazolate subclass, composed of tetrahedrally coordinated Zn²⁺ ions with 2-methylimidazole bidentate linkers⁴⁷) coating on top of a conducting polymer-modified electrode, yielded an enhancement of the ORR via augmented O₂ availability.⁴⁴ On the other hand, we have also reported the growth of mechanically robust MOF films over conductive substrates at neutral pH.^{45,46}

Based on these previous results, herein we studied the incorporation of metallic nanoparticles into the hybrid conducting polymer/MOF nano-organized coatings and explored the possible synergy between these three components aiming to obtain superior performances for the electrocatalyzed ORR in neutral solution. Although the integration of CPs and MOFs has been recently reported for different applications related to the production of supercapacitors and electrocatalysts,^{48–50} to the best of our knowledge, this constitutes the first report on a successful combination of the three components in a composite electrocatalyst for the ORR at neutral pH.

■ MATERIALS AND INSTRUMENTATION

Reagents. Hydrogen hexachloroplatinate (IV), aniline (ANI), 3-aminobenzylamine (ABA), 4-(2-hydroxyethyl)-1-piperazineethanesulfonic acid (HEPES), Zn(NO₃)₂·6H₂O, and 2-methylimidazole (2m-Im) were purchased from Sigma-Aldrich. Sulfuric acid and KCl were obtained from Anedra. Methanol was obtained from Dorwil. All chemicals were used as received without further purification except for aniline that was vacuum distilled. All aqueous solutions were prepared with Milli-Q water.

Instrumentation. Transmission electron microscopy (TEM) characterization was performed using a Tecnai FEI G2 F20 (FEG) microscope operated at 200 kV with a double tilt analytical holder. Samples were placed onto a copper grid as is described next for each case. Energy dispersive X-ray spectroscopy (EDS) were performed for chemical characterization over the sample.

Calculated X-ray diffraction patterns were obtained from Cambridge Crystallographic Data Base (CCDB) and reported ZIF-8 files using Mercury software. Experimental XRD patterns corresponding to the synthesized films were collected at room temperature under ambient conditions on a Phillips X'Pert apparatus.

X-ray photoelectron spectroscopy (XPS) was performed using a SPECS SAGE HR 100 system spectrometer. A Mg K α (1253.6 eV) X-ray source was employed operating at 12.5 kV and 10 mA. Survey spectra were obtained with pass energy of 30 eV whereas 15 eV was employed for detailed spectra. The takeoff angle was 90°. Quantitative analysis of spectra was carried out with Casa XPS 2.3.16 PR 1.6 software, employing Shirley baselines and Gaussian/Lorentzian (30%) product functions. Surface-charging effects were corrected by setting the binding energy (BE) of the main component of the core level C 1s at 284.5 eV.

FTIR spectra were acquired in ATR mode (MIRacle Single Reflection accessory equipped with a diamond prism) using a FTIR Nicolet 480 spectrometer. 128 scans were taken between 500 and 4000 cm^{–1} with a resolution of 4 cm^{–1}. Spectra processing was performed using the software EZ Omnic.

Electrochemical measurements were carried out in a Gamry Reference 600 potentiostat. The experimental setup consisted of a three-electrode Teflon-lined cell with 2 mL volume capacity. The

Scheme 1. Schematic Representation of the Successive Substrate Modification Stages

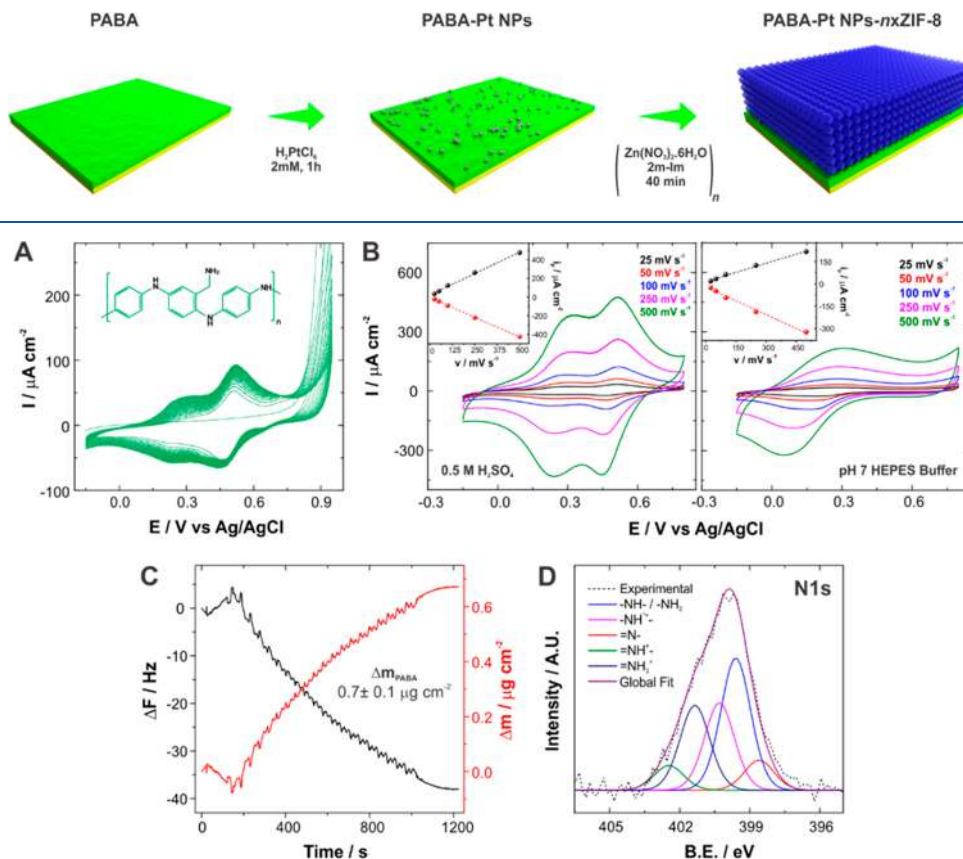


Figure 1. Cyclic voltammograms ($\nu = 50 \text{ mV s}^{-1}$) of PABA electropolymerization (A). Cyclic voltammograms for PABA in H_2SO_4 0.5 M (left) and HEPES 5 mM, 0.1 M KCl (pH 7) (right) at different scan rates (B). Frequency and mass changes upon PABA electropolymerization onto a QCM sensor (C). N 1s XPS spectrum of PABA film (fwhm = 1.5 eV) (D).

counter electrode used was a Pt wire, and Ag/AgCl (3 M NaCl) was used as reference. All the reported potentials are referred to this electrode. Gold electrodes were prepared by Au sputtering on a glass plate. A thin layer of Ti was previously deposited on glass substrates in order to improve the adhesion. The electrodes were cleaned with soft basic piranha solution (1:1:7) of $(\text{NH}_4\text{OH}:\text{H}_2\text{O}_2:\text{H}_2\text{O})$ prior to the electrochemical experiments. Before the electrosynthesis of the conducting copolymer, Au electrodes were cycled in 0.5 M H_2SO_4 between -0.2 and 1.5 V to obtain a clean surface for reproducible electropolymerization conditions. Oxygen reduction tests were performed in HEPES 5 mM 0.1 M KCl solution (pH 7). Oxygen saturated solution was obtained by bubbling pure gas for 30 min before and also during the electrochemistry experiments.

Quartz crystal microbalance (QCM) measurements were performed with a QCM200 setup (Stanford Research Systems) using gold-coated quartz sensors (QCM25 5 MHz, sensitivity factor: $56.6 \text{ Hz cm}^2 \mu\text{g}^{-1}$). Experiments were performed with quiescent solutions in a Teflon cell at room temperature. Electrochemical-QCM experiments were performed with a Gamry ref. 600 potentiostat using a three-electrode Teflon cell. The counter electrode was a Pt wire, and Ag/AgCl was employed as reference.

Substrate Modification. The electrosynthesis of poly(3-aminobenzylamine-*co*-aniline) (PABA) films was performed by cyclic voltammetry in acidic solution as described previously.^{51,52} Briefly, the voltammetric electropolymerization was performed by potential cycling in the presence of 0.07 M ABA and 0.03 M ANI in 0.5 M H_2SO_4 solution from -0.15 to 0.95 V (vs Ag/AgCl) at 50 mV s^{-1} up to 20 voltammetric cycles. By employing this feed ratio, a film composition of approximately 30% in ABA is obtained.^{51,52}

For the incorporation of Pt nanoparticles, PABA-modified Au electrodes were dipped in a 2 mM H_2PtCl_6 solution. After 1 h, the electrodes were rinsed with Milli-Q water.

For the ZIF-8 deposition, the cell was filled with a fresh mixture of $\text{Zn}(\text{NO}_3)_2 \cdot 6\text{H}_2\text{O}$ (25 mM) + 2-methyl-imidazole (50 mM) stock methanolic solutions at room temperature. The frequency change was used to follow ZIF-8 deposition until a plateau was reached (typically after 40 min). The electrode was then rinsed with fresh methanol and dried under N_2 prior to the next cycle. This procedure was repeated until a suitable MOF film thickness was obtained (the films obtained after successive depositions will be referred as $n\text{x-ZIF-8}$, where n is the number growth cycles carried).⁴⁴

TEM Sample Preparation. PABA films were electrosynthesized onto ITO plates ($R_s = 5\text{--}15 \text{ } \Omega \text{ cm}$, Delta Technologies). The plates were previously cleaned with ethanol and Milli-Q water. The electrosynthesis was carried out by cycling the potential at 50 mV s^{-1} between -0.15 and 1.05 V vs SCE (see Figure S1). The electropolymerization solution was 0.03 M ANI + 0.07 M ABA in 0.5 M H_2SO_4 . The area of the working electrode was 1.0 cm^2 . After the synthesis, films were cycled in 3.7 M H_2SO_4 solution for a few minutes and then detached from the ITO plates by applying a potential of -1 V vs SCE. The free-standing films were rinsed with Milli-Q water and then incubated in 2 mM hexachloroplatinic acid solution for 1 h. Finally, they were rinsed several times with water and placed onto a TEM grid.

RESULTS AND DISCUSSION

In this work we describe the effective modification of an electroactive polymer film with two different materials for improving the electrochemical ORR performance at neutral

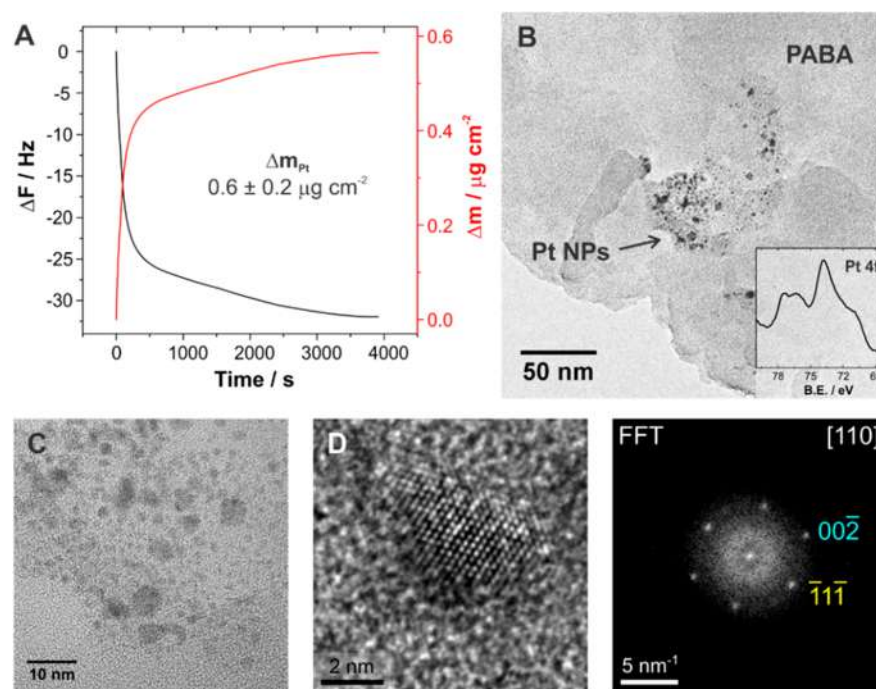


Figure 2. Change in frequency and mass measured by QCM after adding H_2PtCl_6 onto the PABA-modified sensor (A). Bright field image of PABA-Pt NPs film. The inset shows the Pt 4f XPS spectrum of the film (B). HRTEM image of several Pt NPs (C). HRTEM image of a single Pt Nanoparticle and FFT showing that Pt NPs are oriented in the [110] zone axis (D).

pH range. After conducting copolymer electrosynthesis onto the Au substrates, the inclusion of Pt NPs and ZIF-8 was carried in two steps, depicted schematically in Scheme 1. The different modification stages were monitored by AFM and SEM microscopies. These results are presented as Supporting Information as a matter of length (see section 4).

PABA Electropolymerization. It is well-known that PANI electroactivity decreases as pH increases; therefore, the incorporation of PABA constitutes a suitable strategy when an electroactive platform capable of electrocatalysis for the ORR at neutral pH is desired. With this fact in mind, PABA films were first electropolymerized onto Au substrates, and then characterized via E-QCM and XPS techniques.

The voltammograms for the PABA copolymer electropolymerization can be seen in Figure 1A. The PABA-electropolymerization features were previously reported in the literature.^{51,52} Briefly, the peak appearing at about 0.45 V is ascribed as the convolution of the pure poly(3-aminobenzylamine) (0.5 V)⁵² and the so-called “middle peak” of PANI.⁵¹ The peaks placed around 0.7 V correspond to the emeraldine to pernigraniline transitions in Pani. Finally, the peaks observed at 0.22 V are designated as an overlap of the first redox couple for pure poly(3-aminobenzylamine) and PANI (leucoemeraldine to emeraldine transition). The oxidative electropolymerization accounts for the high anodic current values at about 0.9 V.

Further cyclic voltammetry measurements of the conducting copolymer PABA at acidic and neutral pH are presented in Figure 1B. The cyclic voltammetry performance confirms the electroactivity in neutral solutions. The voltammetric response in neutral media presents only one anodic peak because of the overlap of both couples present in acidic medium. In pH 7 buffer the peaks are wider, probably due to the lower electron transfer rate. Moreover, it can be observed a linear change in

the peak current while increasing the sweep rate, which indicates the behavior of a confined reversible redox couple.

Figure 1C shows the frequency and mass changes while performing the PABA electropolymerization onto the QCM sensor. The deposited mass obtained after 20 voltammetry cycles was $0.7 \pm 0.1 \mu\text{g cm}^{-2}$ (three different runs were performed). Taking into account this value and using the previously reported density for PANI (1.33 g cm^{-3}),⁵³ we obtained an estimated thickness for the conducting polymer layer of $\sim 6 \text{ nm}$.

Additional characterization of the conducting copolymer film was performed by XPS. In Figure 1C, the PABA N 1s spectrum is shown. It can be fitted with five components, as reported before (Table S1).^{51,52} The precise determination of the conducting copolymer composition becomes difficult due to the many nitrogen species present. Nevertheless, previous experiments using different monomer feed ratios, and the same electropolymerization conditions, allow for an estimation of 30% molar composition of ABA.^{51,52}

Incorporation of Pt Nanoparticles (Pt NPs). In order to increase the ORR activity of the PABA-modified electrode, Pt loading was explored. The first step of the loading procedure was direct dipping in 2 mM H_2PtCl_6 metal precursor solution for 1 h. The reaction-diffusion approach was explored for Pt reduction; however, dipping the electrode in NaBH_4 reducing agent solution did not yield a detectable improvement of the ORR performance. We hypothesize that using such reducing agent might also compromise polymer film integrity thus affecting its electroactivity. As an alternative and milder procedure to obtain Pt NPs, the substrates were directly washed with water after soaking in metal precursor solution. The incorporation of Pt NPs was therefore achieved by using the conducting polymer film itself as a reducing agent. It has been reported that the driving force for NPs formation is that the conducting polymer, in its oxidized state, can act as an

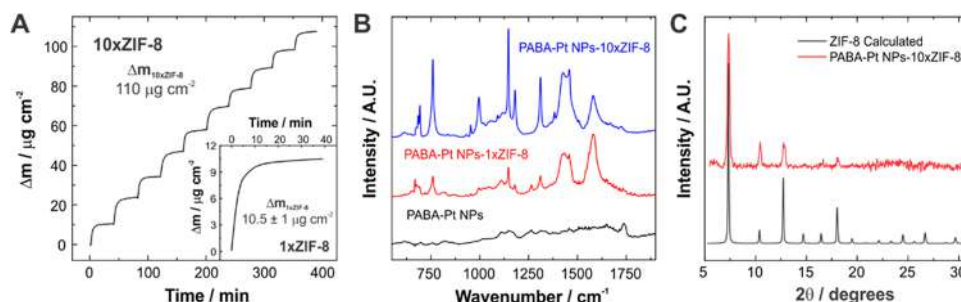


Figure 3. Mass changes measured by QCM of 10 successive ZIF-8 deposition cycles onto a PABA-Pt NPs substrate. The inset shows the time evolution of the mass increment for a given modification step (A). ATR-FTIR spectra of PABA-Pt NPs, PABA-Pt NPs-1xZIF-8, and PABA-Pt NPs-10xZIF-8 modified Au substrates (C). XRD pattern of a PABA-Pt NPs-10xZIF-8 modified substrate (B).

electron donor and the platinum salt as an electron acceptor. Moreover, in acidic media, the oxidized form of the PANI-like polymer may undergo the reduction back to the emeraldine form, thereby promoting further reduction sites.^{6,54}

In order to determine the mass increase occurring when depositing the Pt NPs onto the conducting copolymer, we performed QCM measurements. From 3 different deposition assays, the mass loading obtained was $0.6 \pm 0.2 \mu\text{g cm}^{-2}$ (Figure 2A). After potential cycling in buffer solution to eliminate the excess of precursors within the films, washing with pure water and drying with N_2 , the mass increment due to Pt deposition was determined to be $0.46 \pm 0.15 \mu\text{g cm}^{-2}$.

The formation of Pt NPs was characterized by TEM. In this case, the TEM sample was prepared using free-standing PABA films, which were immersed in the precursor solution for 1 h, and then washed with water. Figure 2B shows a bright field image of this film. The presence of metallic NPs is directly observed, meaning that Pt NPs can be readily formed by the direct contact of the electroactive film with PtCl_6^{2-} .

It is well-known that electron beams can reduce metal compounds producing metallic NPs by irradiation damage,^{55,56} therefore, this effect must be carefully considered in order to obtain information on the as-synthesized film. In each case, images were acquired with different electron beam exposure time (radiation doses), and information was used only after confirming no size increase and no appearance of new nanoparticles (see SI).

The inset in Figure 2B shows the XPS Pt 4f core level spectrum of PABA-Pt NPs film. The XPS data could be fitted with two components ascribed as metallic Pt at about 71.2 eV and other oxidized component at about 73.5 eV, assigned to Pt atoms having loss of electron density.⁵ HRTEM images show Pt nanoparticles with size up to 10 nm (Figure 2C). Figure 2D shows that the atomic planes can be indexed as families {111} and {200} of fcc structure of metallic Pt (see also Supporting Information, Figure S2). Therefore, in agreement with the XPS measurements, the TEM characterization clearly shows the presence of metallic Pt NPs.

ZIF-8 Anchoring. It was shown that ZIF-8 can selectively take up O_2 from buffer solutions, thus increasing the overall ORR composite performance.⁴⁴ By making use of this strategy, the last step of the substrate modification consisted of the deposition via 1 to 10 sequential growth cycles ZIF-8 MOF from methanolic precursor solutions onto the PABA-Pt NPs film, according to previously reported procedures.^{57,58} After the modification with Pt NPs, the growth of a ZIF-8 film on top of the substrates was performed for about 40 min for each cycle (n x-ZIF-8). The deposition was monitored *in situ* with

QCM. After deposition, the precursor's solution was discharged and the substrate was washed with pure methanol and dried by N_2 flux before performing further characterization measurements or electrochemical tests.

In Figure 3A, the change in mass measured by QCM for 10 successive ZIF-8 growth cycles onto PABA-Pt NPs is shown. The inset shows time evolution of mass increment for one growth cycle. It can be noted that the mass change for every deposition step is homogeneous in the 10 cycles performed.

An estimation of the thickness of the MOF films can be carried out as follows. From the mass changes during the MOF deposition in solution (Δm_{sol}) and the mass determined for the corresponding dried MOF layer (m_{MOF}), a correlation of $m_{\text{MOF}} = 0.35 \Delta m_{\text{sol}}$ was obtained. Moreover, the AFM determination of the thickness for a dried MOF mass of $2.4 \mu\text{g cm}^{-2}$ yielded 28 nm (Figure S6), meaning a film mean density of 0.86 g cm^{-3} . Thus, using this density, approximate thickness values of 43 and 450 nm were computed for 1x- and 10x-ZIF-8 coatings in Figure 3A, respectively.

In order to confirm the presence of the MOF deposited onto the already Pt-modified polymer layer, we performed FTIR measurements. Figure 3B shows the ATR-mode FTIR spectra of PABA-Pt NPs, PABA-Pt NPs-1xZIF-8, and PABA-Pt NPs-10xZIF-8 substrates. The PABA-Pt spectrum shows very weak bands (due to the small mass of polymer electro synthesized onto the Au substrate) in the zone ranging from 1100 to 1750 cm^{-1} , ascribed as C–N and C–C stretching modes of quinoid and benzenic rings present in the polyaniline-like structure.^{59,60} After 1 cycle of MOF deposition, the spectrum shows typical features of ZIF-8, most of them corresponding to imidazole ring vibrations. The peak appearing at 1585 cm^{-1} is assigned as C=N stretching, while the intense band in the zone between 1350 and 1500 cm^{-1} is ascribed to the entire imidazole ring stretching mode. The bands in the 900–1350 cm^{-1} region can be identified as in-plane ring bending, while those appearing below 800 cm^{-1} correspond to out-of-plane bending.^{61,62} After 10 MOF growth cycles, the bands become stronger and acquire a better definition, accounting for the higher amount of material on the film.

Figure 3C shows the XRD pattern of a PABA-Pt NPs-10xZIF-8 modified electrode together with the calculated pattern for ZIF-8. In this case, a 10xZIF-8 modification was needed onto the PABA-Pt substrate in order to acquire the necessary thickness for the diffraction peaks to be observed. The peaks belonging to (110), (200), (211), and (222) Miller indices, appearing at 2θ values of 7.3°, 10.2°, 12.6°, and 17.8°, respectively,⁴⁷ can be clearly observed in the PABA-Pt-10xZIF-8 modified substrate. These results confirm the effective

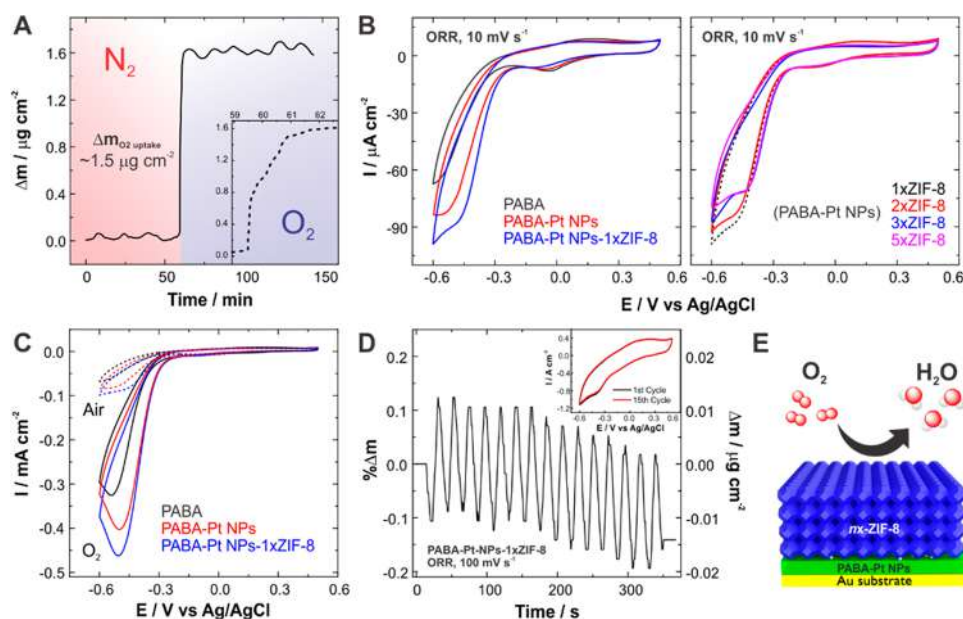


Figure 4. Change in mass measured by QCM upon switching from N_2 -saturated to O_2 -saturated solutions for a PABA-Pt NPs-10xZIF-8 modified substrate (A). Cyclic voltammograms for PABA, PABA-Pt NPs, and PABA-Pt NPs-1xZIF-8 (left); and for PABA-Pt NPs- n xZIF-8 (right) in air-saturated HEPES 5 mM 0.1 M KCl solution; $\nu = 10 \text{ mV s}^{-1}$ (B). Cyclic voltammograms for PABA, PABA-Pt NPs, and PABA-Pt NPs-1xZIF-8 in air- and O_2 -saturated HEPES 5 mM 0.1 M KCl solution; $\nu = 10 \text{ mV s}^{-1}$ (C). Relative and total mass change upon 15 consecutive voltammetric cycles for a PABA-Pt-1xZIF-8 modified electrode, in air-saturated HEPES 5 mM 0.1 M KCl solution; $\nu = 100 \text{ mV s}^{-1}$ (D). Schematic representation of the modified substrate for ORR (E).

anchoring and, more importantly, the crystalline structure of the deposited ZIF-8 film onto the PABA-Pt NPs layer.

To evaluate the MOF layer preferential uptake of O_2 over N_2 from aqueous solutions, QCM measurements were performed by flowing N_2 and O_2 -saturated buffer solutions through the QCM cell using a PABA-Pt NPs-10xZIF-8 modified substrate under atmospheric pressure at room temperature. Ten cycles of MOF deposition were employed for achieving more sensibility in the QCM experiment, as the mass change caused by the differential adsorption of molecular oxygen is proportional to the amount of MOF present.⁴⁴

For the determination of the differential oxygen uptake from aqueous solution, the MOF-modified QCM sensor was first equilibrated in a N_2 -saturated 5 mM HEPES in 0.1 M KCl (pH 7) solution by continuous flux for 1 h. Then, this buffer was replaced by O_2 -saturated buffer, which continued flowing for 1 h. The mass change was computed from the difference of the average resonance frequency in equilibrium at each condition (Figure 4A). An increment of $\approx 1.5 \mu\text{g cm}^{-2}$ was obtained for the change from N_2 -saturated to O_2 -saturated buffer. This mass increment reinforces the idea of a preferential uptake of O_2 within the MOF, which increases the amount of reagent available for the electrochemical reaction, causing a preconcentration effect.

Electrochemistry Performance. The voltammetric responses of the Oxygen Reduction Reaction, PABA, PABA-Pt NPs, and PABA-Pt NPs-1xZIF-8 electrodes in air-bubbled pH 7 buffer are shown in Figure 4B left. For the PABA-modified electrode, the voltammetric wave at approximately -0.27 V corresponds to the ORR on this electrode at neutral pH. The activity of PABA toward the ORR was previously reported and it is believed to occur by a two-electron reduction with H_2O_2 as product.⁴⁴

As can be noted in Figure 4B (left), after the deposition of the Pt NPs, the voltammetric O_2 reduction wave of the

modified electrode is clearly increased. Moreover, it can be seen that the ORR wave onset potential is shifted in approximately 70 mV toward positive potentials (from -0.27 to -0.2 V approximately) due to electrocatalytic effect of the Pt NPs. These results also confirm the effective incorporation of the Pt NPs onto the conducting polymer and its enhancement of the ORR.

Furthermore, after the deposition of a ZIF-8 layer onto the modified electrode, the voltammetric O_2 reduction wave was also notoriously increased. In this case, no shift is observed in the voltammetric peak potential compared with uncovered PABA-Pt electrode, which indicates that there is no additional electrocatalytic activity of the composite electrode material, as previously reported. This means that the MOF shows no electroactivity, but rather acts as a high surface area oxygen reservoir in close contact with electroactive centers on the film without blocking the arrival of O_2 molecules. It should be noted that no enhancement was observed after treatment of the PABA-modified electrode with methanol for 40 min (see Figure S5). This blank experiment confirms that the enhanced activity cannot be assigned to chemical effects introduced in the polymer layer due to a solvent effect.

By the comparison of the integrated charge obtained from the ORR waves for the electrode after each modification step, it is possible to conclude that the enhancement produced by the incorporation of the MOF layer reaches the 66% of the increment due to the addition of the electrocatalytic Pt-NPs (see SI). The enhancement observed is very remarkable taking into account that ZIF-8 MOF is electrochemically inactive, and nonconductive, which could cause additional blocking effects on the electrode surface.⁵⁸

The effect of a MOF layer thickness increase in the ORR performance was also explored by cyclic voltammetry. Figure 4B (right) shows the voltammetric response of PABA-Pt NPs electrodes after successive ZIF-8 deposition cycles. As can be

seen from the cathodic peak of the voltammograms, there is no further enhancement after performing additional growth cycles. The peak current diminishes for 2x-, 3x-, and 5x-ZIF-8 layers. This fact can be ascribed to either a loss in O₂ transport efficiency from bulk solution toward the electroactive material through the MOF layer porosity, and/or slower transport of ions and solvent in the film as it becomes thicker.

Interestingly, the enhancement of the ORR current by the MOF layer is yet appreciable in O₂-saturated solutions (Figure 4C). Although the relative enhancement is lower than in air saturation conditions, it has still a remarkable value, reaching the 43% of the increment produced by the Pt-NPs (Figure S10).

The stability of the assembled composite material was further assessed by means of E-QCM experiments. An E-QCM setup was used in order to establish whether mass loss of the composite PABA-Pt-1xZIF-8 electrode occurs during the potential cycling. Figure 4D shows the mass changes upon ORR conditions cycling at a relatively high sweep rate (100 mV s⁻¹). The inset shows both voltammetric curves for the first and the 15th cycles. It can be stated that performance is maintained during the high-rate ORR cycling. Although there are mass variations during the potential cycling probably caused by the oxidation/reduction processes in the electroactive polymer, the net change after the cycling is negligible (-0.1%), pointing thus to a structural stability of film architecture under the experimental conditions explored. Additional voltammetric studies showing the good mechanical stability of the MOF coating are presented in the SI file.

CONCLUSIONS

We presented the rational integration of three different building blocks into a functional interfacial architecture by a simple sequential procedure. We first electrosynthesized Pani-like electroactive polymer films. Then, the incorporation of metallic nanoparticles on these films was achieved by simple immersion in the precursor solution by employing the redox centers in the electroactive polymer as reducing agents. The formation of metallic Pt nanoparticles within the electroactive films was proved by XPS and TEM analysis. Finally, a stable layer of a micro/mesoporous metal-organic material was added over the electroactive blocks by using the amine moieties as anchoring sites for the ZIF-8 MOF growth.

The increased electroactivity of PABA compared to Pani in neutral solutions allows the effective electrical connectivity of the Pt NPs dispersed within the polymeric matrix, which is an essential requirement for their actuation as electrocatalyzers. The electrocatalytic effect of adding the NPs on the ORR was observed as an increase in the cathodic current and a shift of the onset potential.

Moreover, the ZIF-8 MOF coating results to be chemical and mechanically stable in neutral buffer solution and its integration on top of the electroactive material yields an enhancement of the ORR at pH 7. As proved by QCM and voltammetric experiments, the incorporation of ZIF-8 nanocrystals as an external coating does not only allow the ionic transport within its interparticle interstices but also selectively preconcentrates O₂ from solution. Thus, the MOF coating increases the amount of O₂ available for the electrochemical reaction on the metallic nanoparticles immersed in the electroactive film, yielding enhanced ORR currents.

The present work constitutes a step forward in the construction of complex interfaces by incorporating electro-

catalytic nanomaterials to a previously reported conducting polymer-MOF hybrid modified electrode.⁴⁴ Results presented here indicate that the enhancement of the ORR current produced by the integration of the O₂-preconcentrating MOF can be additively conjugated with the electrocatalytic effect of a third component. In principle, this proof-of-concept could be extended to other electrocatalytic materials and even other type of MOFs, provided that two basic conditions are met: the MOF can be effectively anchored to the base material (to guarantee the electrochemical stability), and the MOF coating is able to allow the ionic transport within its mesoporosity.

Finally, the synthetic approach presented here illustrates how the rational integration of diverse building blocks having particular properties (electroactivity, catalytic activity, gas-selective adsorption) into multifunctional electroactive architectures can push the boundaries of nanoarchitectonics for the production of more efficient electrochemical systems.^{63,64}

ASSOCIATED CONTENT

Supporting Information

The Supporting Information is available free of charge on the ACS Publications website at DOI: 10.1021/acsae.8b01021.

Further electrochemical characterization, detailed XPS, TEM, AFM, and SEM analysis (PDF)

AUTHOR INFORMATION

Corresponding Authors

*E-mail: mrafti@quimica.unlp.edu.ar.

*E-mail: wmarmi@inifta.unlp.edu.ar.

ORCID

Gonzalo E. Fenoy: 0000-0003-4336-4843

Matias Rafti: 0000-0003-3393-358X

Waldemar A. Marmisollé: 0000-0003-0031-5371

Omar Azzaroni: 0000-0002-5098-0612

Notes

The authors declare no competing financial interest.

ACKNOWLEDGMENTS

The authors acknowledge financial support from ANPCyT (PICT-2013-0905, PICT-2015-0239, PICT-2016-1680), Universidad Nacional de La Plata (PPID-X016), CONICET (PIP 11220130100619CO). AFM measurements and analysis by Dr. Catalina von Bilderling is greatly appreciated. J.A., M.R., W.M., and O.A. are CONICET staff members. G.E.F. and J.S. gratefully acknowledge a scholarship from CONICET.

REFERENCES

- (1) Downes, C. A.; Marinescu, S. C. Electrocatalytic Metal-Organic Frameworks for Energy Applications. *ChemSusChem* **2017**, *10*, 4374–4392.
- (2) Seh, Z. W.; Kibsgaard, J.; Dickens, C. F.; Chorkendorff, I.; Nørskov, J. K.; Jaramillo, T. F. Combining Theory and Experiment in Electrocatalysis: Insights into Materials Design. *Science* **2017**, *355*, eaad4998.
- (3) Nie, Y.; Li, L.; Wei, Z. Recent Advancements in Pt and Pt-Free Catalysts for Oxygen Reduction Reaction. *Chem. Soc. Rev.* **2015**, *44*, 2168–2201.
- (4) Shao, M.; Chang, Q.; Dodelet, J.-P.; Chenitz, R. Recent Advances in Electrocatalysts for Oxygen Reduction Reaction. *Chem. Rev.* **2016**, *116*, 3594–3657.
- (5) Fenoy, G. E.; Maza, E.; Zelaya, E.; Marmisollé, W. A.; Azzaroni, O. Layer-by-Layer Assemblies of Highly Connected Polyelectrolyte

Capped-Pt Nanoparticles for Electrocatalysis of Hydrogen Evolution Reaction. *Appl. Surf. Sci.* **2017**, *416*, 24–32.

(6) Han, J.; Wang, M.; Hu, Y.; Zhou, C.; Guo, R. Conducting Polymer-Noble Metal Nanoparticle Hybrids: Synthesis Mechanism Application. *Prog. Polym. Sci.* **2017**, *70*, 52–91.

(7) Mondal, S.; Malik, S. Easy Synthesis Approach of Pt-Nanoparticles on Polyaniline Surface: An Efficient Electro-Catalyst for Methanol Oxidation Reaction. *J. Power Sources* **2016**, *328*, 271–279.

(8) Kim, K.; Ahn, H.; Park, M. J. Highly Catalytic Pt Nanoparticles Grown in Two-Dimensional Conducting Polymers at the Air–Water Interface. *ACS Appl. Mater. Interfaces* **2017**, *9*, 30278–30282.

(9) Heinze, J.; Frontana-Urbe, B. a.; Ludwigs, S. Electrochemistry of Conducting Polymers—Persistent Models and New Concepts. *Chem. Rev.* **2010**, *110*, 4724–4771.

(10) Xu, P.; Han, X.; Zhang, B.; Du, Y.; Wang, H.-L. Multifunctional Polymer–metal Nanocomposites via Direct Chemical Reduction by Conjugated Polymers. *Chem. Soc. Rev.* **2014**, *43*, 1349–1360.

(11) Furukawa, H.; Cordova, K. E.; O’Keeffe, M.; Yaghi, O. M. The Chemistry and Applications of Metal-Organic Frameworks. *Science* **2013**, *341*, 1230444–1230444.

(12) Falcaro, P.; Ricco, R.; Doherty, C. M.; Liang, K.; Hill, A. J.; Styles, M. J. MOF Positioning Technology and Device Fabrication. *Chem. Soc. Rev.* **2014**, *43*, 5513–5560.

(13) Wang, H.; Zhu, Q.-L.; Zou, R.; Xu, Q. Metal-Organic Frameworks for Energy Applications. *Chem.* **2017**, *2*, 52–80.

(14) Li, B.; Wen, H.; Cui, Y.; Zhou, W.; Qian, G.; Chen, B. *Emerging Multifunctional Metal – Organic Framework Materials*, 2016.

(15) Farha, O. K.; Eryazici, I.; Jeong, N. C.; Hauser, B. G.; Wilmer, C. E.; Sarjeant, A. a.; Snurr, R. Q.; Nguyen, S. T.; Yazaydin, A. Ö.; Hupp, J. T. Metal–Organic Framework Materials with Ultrahigh Surface Areas: Is the Sky the Limit? *J. Am. Chem. Soc.* **2012**, *134*, 15016–15021.

(16) Huang, Y.; Liang, J.; Wang, X.; Cao, R. Multifunctional Metal–organic Framework Catalysts: Synergistic Catalysis and Tandem Reactions. *Chem. Soc. Rev.* **2017**, *46*, 126–157.

(17) Chang, T.-H.; Kung, C.-W.; Chen, H.-W.; Huang, T.-Y.; Kao, S.-Y.; Lu, H.-C.; Lee, M.-H.; Boopathi, K. M.; Chu, C.-W.; Ho, K.-C. Planar Heterojunction Perovskite Solar Cells Incorporating Metal-Organic Framework Nanocrystals. *Adv. Mater.* **2015**, *27*, 7229–7235.

(18) Liu, J.; Zhou, W.; Liu, J.; Howard, I.; Kilibarda, G.; Schlabach, S.; Coupry, D.; Addicoat, M.; Yoneda, S.; Tsutsui, Y.; Sakurai, T.; Seki, S.; Wang, Z.; Lindemann, P.; Redel, E.; Heine, T.; Wöll, C. Photoinduced Charge-Carrier Generation in Epitaxial MOF Thin Films: High Efficiency as a Result of an Indirect Electronic Band Gap? *Angew. Chem., Int. Ed.* **2015**, *54*, 7441–7445.

(19) Zhang, Z.; Yao, Z.-Z.; Xiang, S.; Chen, B. Perspective of Microporous Metal–organic Frameworks for CO₂ Capture and Separation. *Energy Environ. Sci.* **2014**, *7*, 2868.

(20) Wu, D.; Guo, Z.; Yin, X.; Pang, Q.; Tu, B.; Zhang, L.; Wang, Y.-G.; Li, Q. Metal-Organic Frameworks as Cathode Materials for Li-O₂ Batteries. *Adv. Mater.* **2014**, *26*, 3258–3262.

(21) Fracaroli, A. M.; Furukawa, H.; Suzuki, M.; Dodd, M.; Okajima, S.; Gándara, F.; Reimer, J. A.; Yaghi, O. M. Metal–Organic Frameworks with Precisely Designed Interior for Carbon Dioxide Capture in the Presence of Water. *J. Am. Chem. Soc.* **2014**, *136*, 8863–8866.

(22) Xiang, S.; He, Y.; Zhang, Z.; Wu, H.; Zhou, W.; Krishna, R.; Chen, B. Microporous Metal-Organic Framework with Potential for Carbon Dioxide Capture at Ambient Conditions. *Nat. Commun.* **2012**, *3*, 954–959.

(23) Alkordi, M. H.; Liu, Y.; Larsen, R. W.; Eubank, J. F.; Eddaoudi, M. Zeolite-like Metal–Organic Frameworks as Platforms for Applications: On Metalloporphyrin-Based Catalysts. *J. Am. Chem. Soc.* **2008**, *130*, 12639–12641.

(24) Yuan, S.; Zou, L.; Qin, J.; Li, J.; Huang, L.; Feng, L.; Wang, X.; Bosch, M.; Alsalmeh, A.; Cagin, T.; Zhou, H.-C. Construction of Hierarchically Porous Metal–organic Frameworks through Linker Labelization. *Nat. Commun.* **2017**, *8*, 15356.

(25) Hou, C.; Wang, Y.; Ding, Q.; Jiang, L.; Li, M.; Zhu, W.; Pan, D.; Zhu, H.; Liu, M. Facile Synthesis of Enzyme-Embedded Magnetic Metal–organic Frameworks as a Reusable Mimic Multi-Enzyme System: Mimetic Peroxidase Properties and Colorimetric Sensor. *Nanoscale* **2015**, *7*, 18770–18779.

(26) Qiu, X.; Zhong, W.; Bai, C.; Li, Y. Encapsulation of a Metal–Organic Polyhedral in the Pores of a Metal–Organic Framework. *J. Am. Chem. Soc.* **2016**, *138*, 1138–1141.

(27) Aijaz, A.; Xu, Q. Catalysis with Metal Nanoparticles Immobilized within the Pores of Metal–Organic Frameworks. *J. Phys. Chem. Lett.* **2014**, *5*, 1400–1411.

(28) Stassen, I.; Styles, M.; Greci, G.; van Gorp, H.; Vanderlinden, W.; Feyter, S. De; Falcaro, P.; Vos, D. De; Vereecken, P.; Ameloot, R. Chemical Vapour Deposition of Zeolitic Imidazolate Framework Thin Films. *Nat. Mater.* **2016**, *15*, 304–310.

(29) Jahan, M.; Bao, Q.; Loh, K. P. Electrocatalytically Active Graphene-Porphyrin MOF Composite for Oxygen Reduction Reaction. *J. Am. Chem. Soc.* **2012**, *134*, 6707–6713.

(30) Huang, X.; Zheng, B.; Liu, Z.; Tan, C.; Liu, J.; Chen, B.; Li, H.; Chen, J.; Zhang, X.; Fan, Z.; Zhang, W.; Guo, Z.; Huo, F.; Yang, Y.; Xie, L.-H.; Huang, W.; Zhang, H. Coating Two-Dimensional Nanomaterials with Metal–Organic Frameworks. *ACS Nano* **2014**, *8*, 8695–8701.

(31) Yu, J.; Mu, C.; Yan, B.; Qin, X.; Shen, C.; Xue, H.; Pang, H. Nanoparticle/MOF Composites: Preparations and Applications. *Mater. Horiz.* **2017**, *4*, 557–569.

(32) Tang, J.; Salunkhe, R. R.; Zhang, H.; Malgras, V.; Ahamad, T.; Alshehri, S. M.; Kobayashi, N.; Tominaka, S.; Ide, Y.; Kim, J. H.; Yamauchi, Y. Bimetallic Metal-Organic Frameworks for Controlled Catalytic Graphitization of Nanoporous Carbons. *Sci. Rep.* **2016**, *6*, 30295.

(33) Wade, C. R.; Li, M.; Dincă, M. Facile Deposition of Multicolored Electrochromic Metal-Organic Framework Thin Films. *Angew. Chem., Int. Ed.* **2013**, *52*, 13377–13381.

(34) Morozan, A.; Jaouen, F. Metal Organic Frameworks for Electrochemical Applications. *Energy Environ. Sci.* **2012**, *5*, 9269.

(35) Sun, L.; Campbell, M. G.; Dincă, M. Electrically Conductive Porous Metal-Organic Frameworks. *Angew. Chem., Int. Ed.* **2016**, *55*, 3566–3579.

(36) Aquino Neto, S.; Milton, R. D.; Hickey, D. P.; De Andrade, A. R.; Minter, S. D. Membraneless Enzymatic Ethanol/O₂fuel Cell: Transitioning from an Air-Breathing Pt-Based Cathode to a Bilirubin Oxidase-Based Biocathode. *J. Power Sources* **2016**, *324*, 208–214.

(37) Chang, Z.; Yang, Y.; Li, M.; Wang, X.; Wu, Y. Green Energy Storage Chemistries Based on Neutral Aqueous Electrolytes. *J. Mater. Chem. A* **2014**, *2*, 10739–10755.

(38) Santoro, C.; Arbizzani, C.; Erable, B.; Ieropoulos, I. Microbial Fuel Cells: From Fundamentals to Applications. A Review. *J. Power Sources* **2017**, *356*, 225–244.

(39) Zhang, Z.; Chen, Y.; Xu, X.; Zhang, J.; Xiang, G.; He, W.; Wang, X. Well-Defined Metal-Organic Framework Hollow Nanocages. *Angew. Chem.* **2014**, *126*, 439–443.

(40) Li, Z.; Yu, R.; Huang, J.; Shi, Y.; Zhang, D.; Zhong, X.; Wang, D.; Wu, Y.; Li, Y. Platinum–nickel Frame within Metal-Organic Framework Fabricated in Situ for Hydrogen Enrichment and Molecular Sieving. *Nat. Commun.* **2015**, *6*, 8248.

(41) Xu, H.; Hu, J.; Wang, D.; Li, Z.; Zhang, Q.; Luo, Y.; Yu, S.; Jiang, H. Visible-Light Photoreduction of CO₂ in a Metal–Organic Framework: Boosting Electron–Hole Separation via Electron Trap States. *J. Am. Chem. Soc.* **2015**, *137*, 13440–13443.

(42) Aijaz, A.; Fujiwara, N.; Xu, Q. From Metal–Organic Framework to Nitrogen-Decorated Nanoporous Carbons: High CO₂ Uptake and Efficient Catalytic Oxygen Reduction. *J. Am. Chem. Soc.* **2014**, *136*, 6790–6793.

(43) Liu, Q.; Low, Z.-X.; Li, L.; Razmjou, A.; Wang, K.; Yao, J.; Wang, H. ZIF-8/Zn₂GeO₄ Nanorods with an Enhanced CO₂ Adsorption Property in an Aqueous Medium for Photocatalytic Synthesis of Liquid Fuel. *J. Mater. Chem. A* **2013**, *1*, 11563.

- (44) Rafti, M.; Marmisollé, W. A.; Azzaroni, O. Metal–Organic Frameworks Help Conducting Polymers Optimize the Efficiency of the Oxygen Reduction Reaction in Neutral Solutions. *Adv. Mater. Interfaces* **2016**, *3*, 1600047.
- (45) Tuninetti, J. S.; Rafti, M.; Azzaroni, O. Early Stages of ZIF-8 Film Growth: The Enhancement Effect of Primers Exposing Sulfonate Groups as Surface-Confined Nucleation Agents. *RSC Adv.* **2015**, *5*, 73958–73962.
- (46) Rafti, M.; Allegretto, J. A.; Segovia, G. M.; Tuninetti, J. S.; Giussi, J. M.; Bindini, E.; Azzaroni, O. Metal–organic Frameworks Meet Polymer Brushes: Enhanced Crystalline Film Growth Induced by Macromolecular Primers. *Mater. Chem. Front* **2017**, *1*, 2256–2260.
- (47) Park, K. S.; Ni, Z.; Cote, A. P.; Choi, J. Y.; Huang, R.; Uribe-Romo, F. J.; Chae, H. K.; O’Keeffe, M.; Yaghi, O. M. Exceptional Chemical and Thermal Stability of Zeolitic Imidazolate Frameworks. *Proc. Natl. Acad. Sci. U. S. A.* **2006**, *103*, 10186–10191.
- (48) Khalid, M.; Honorato, A. M. B.; Varela, H.; Dai, L. Multifunctional Electrocatalysts Derived from Conducting Polymer and Metal Organic Framework Complexes. *Nano Energy* **2018**, *45*, 127–135.
- (49) Xu, X.; Tang, J.; Qian, H.; Hou, S.; Bando, Y.; Hossain, M. S. A.; Pan, L.; Yamauchi, Y. Three-Dimensional Networked Metal–Organic Frameworks with Conductive Polypyrrole Tubes for Flexible Supercapacitors. *ACS Appl. Mater. Interfaces* **2017**, *9*, 38737–38744.
- (50) Le Ouay, B.; Boudot, M.; Kitao, T.; Yanagida, T.; Kitagawa, S.; Uemura, T. Nanostructuring of PEDOT in Porous Coordination Polymers for Tunable Porosity and Conductivity. *J. Am. Chem. Soc.* **2016**, *138*, 10088–10091.
- (51) Fenoy, G. E.; Giussi, J. M.; von Bilderling, C.; Maza, E. M.; Pietrasanta, L. I.; Knoll, W.; Marmisollé, W. A.; Azzaroni, O. Reversible Modulation of the Redox Activity in Conducting Polymer Nanofilms Induced by Hydrophobic Collapse of a Surface-Grafted Polyelectrolyte. *J. Colloid Interface Sci.* **2018**, *518*, 92–101.
- (52) Marmisollé, W. A.; Gregurec, D.; Moya, S.; Azzaroni, O. Polyanilines with Pendant Amino Groups as Electrochemically Active Copolymers at Neutral pH. *ChemElectroChem* **2015**, *2*, 2011–2019.
- (53) Stejskal, J.; Gilbert, R. G. Polyaniline. Preparation of a Conducting Polymer (IUPAC Technical Report). *Pure Appl. Chem.* **2002**, *74*, 857.
- (54) O’Mullane, A. P.; Dale, S. E.; Macpherson, J. V.; Unwin, P. R. Fabrication and Electrocatalytic Properties of Polyaniline/Pt Nanoparticle Composites. *Chem. Commun.* **2004**, *2*, 1606.
- (55) Corthey, G.; Giovanetti, L. J.; Ramallo-López, J. M.; Zelaya, E.; Rubert, A. A.; Benitez, G. A.; Requejo, F. G.; Fonticelli, M. H.; Salvarezza, R. C. Synthesis and Characterization of Gold@gold(I)-Thiomalate Core@shell Nanoparticles. *ACS Nano* **2010**, *4*, 3413–3421.
- (56) Kim, J.-U.; Cha, S.-H.; Shin, K.; Jho, J. Y.; Lee, J.-C. Synthesis of Gold Nanoparticles from Gold(I)–Alkanethiolate Complexes with Supramolecular Structures through Electron Beam Irradiation in TEM. *J. Am. Chem. Soc.* **2005**, *127*, 9962–9963.
- (57) Hou, C.; Xu, Q.; Peng, J.; Ji, Z.; Hu, X. (110)-Oriented ZIF-8 Thin Films on ITO with Controllable Thickness. *ChemPhysChem* **2013**, *14*, 140–144.
- (58) Tuninetti, J. S.; Rafti, M.; Andrieu-Brunsen, A.; Azzaroni, O. Molecular Transport Properties of ZIF-8 Thin Films in Aqueous Environments: The Critical Role of Intergrain Mesoporosity as Diffusional Pathway. *Microporous Mesoporous Mater.* **2016**, *220*, 253–257.
- (59) Ping, Z.; Nauer, G. E.; Neugebauer, H.; Theiner, J.; Neckel, A. In Situ Fourier Transform Infrared Attenuated Total Reflection (FTIR-ATR) Spectroscopic Investigations on the Base-Acid Transitions of Leucoemeraldine. *Electrochim. Acta* **1997**, *42*, 1693–1700.
- (60) Furukawa, Y.; Ueda, F.; Hyodo, Y.; Harada, I.; Nakajima, T.; Kawagoe, T. Vibrational Spectra and Structure of Polyaniline. *Macromolecules* **1988**, *21*, 1297–1305.
- (61) Hu, Y.; Kazemian, H.; Rohani, S.; Huang, Y.; Song, Y. In Situ High Pressure Study of ZIF-8 by FTIR Spectroscopy. *Chem. Commun.* **2011**, *47*, 12694.
- (62) Lu, G.; Hupp, J. T. Metal Organic Frameworks as Sensors A ZIF-8 Based Fabry Perot Device as a Selective Sensor for Chemical Vapours and Gases. *J. Am. Chem. Soc.* **2010**, *132*, 7832–7833.
- (63) Khan, A. H.; Ghosh, S.; Pradhan, B.; Dalui, A.; Shrestha, L. K.; Acharya, S.; Ariga, K. Two-Dimensional (2D) Nanomaterials towards Electrochemical Nanoarchitectonics in Energy-Related Applications. *Bull. Chem. Soc. Jpn.* **2017**, *90*, 627–648.
- (64) Kim, J.; Kim, J. H.; Ariga, K. Redox-Active Polymers for Energy Storage Nanoarchitectonics. *Joule* **2017**, *1*, 739–768.